A predictive penetrative fracture mapping method from regional potential field and geologic datasets, southwest Colorado Plateau, U.S.A.

Mark E. Gettings and Mark W. Bultman

U.S. Geological Survey, 520 N. Park Ave., Tucson, AZ 85719, USA

Some aquifers of the southwest Colorado Plateau, U.S.A., are deeply buried and overlain by several impermeable units, and thus recharge to the aquifer is probably mainly by seepage down penetrative fracture systems. This purpose of this study was to develop a method to map the location of candidate deep penetrative fractures over a 120,000 km^2 area using gravity and aeromagnetic anomaly data together with surficial fracture data. The resulting database constitutes a spatially registered estimate of recharge location. Candidate deep fractures were obtained by spatial correlation of horizontal gradient and analytic signal maxima of gravity and magnetic anomalies vertically with major surficial lineaments obtained from geologic, topographic, side-looking airborne radar, and satellite imagery. The maps define a sub-set of possible penetrative fractures because of limitations of data coverage and the analysis technique. The data and techniques employed do not yield any indication as to whether fractures are open or closed. Correlations were carried out using image processing software in such a way that every pixel on the resulting grids was coded to uniquely identify which datasets correlated. The technique correctly identified known deep fracture systems and many new ones. Maps of the correlations also define in detail the tectonic fabrics of the southwestern Colorado Plateau.

Key words: Fracture recharge geospatial correlation potential fields tectonic fabric.

1. Introduction

The Colorado Plateau south of the Colorado River and west of the Little Colorado River (Fig. 1) is the source area for ground water recharge to the deep aquifers feeding the springs and seeps on the south side of the Grand Canyon (Robson and Banta, 1995). In particular, the Mississippian Redwall Limestone, with its fracturing and karsts, is an important deep aquifer. This part of the Plateau is sparsely populated and relatively undeveloped with few deep boreholes, and thus little is known of its geology and hydrology except at a regional scale. Because several of the aquifers are beneath essentially impermeable shale formations up section, most recharge is believed to be down penetrative fractures rather than by interstratal percolation. Thus, knowledge of the deep penetrative fracture distribution may be helpful in managing the groundwater resources. The objective of this study was to produce a set of maps of candidate deep fractures for the southwestern Colorado Plateau derived from vertical spatial correlation of surficial fractures with the lineaments of deep structure derived from analysis of gravity and aeromagnetic data (Gettings, 2003, 2003a). On the maps of candidate deep fracture locations, areas of high density or spatial frequency of correlations provide an estimate of where recharge potential is more favorable.

Six 1:250,000-scale quadrangles covering the southwest portion of the Colorado Plateau in Arizona constituted the study area (Fig. 1). The area includes some regions north of the Colorado River and parts of the Transition Zone and Basin and Range provinces. An area of one 1:250,000 sheet approximately centered on 112° west longitude and 36° north latitude is here designated the "focus area" (Fig. 1) and is made up of four quarters of the surrounding four quadrangles. Within the focus area, a line drawing was hand drawn from the correlation maps produced for all quadrangles. Although it does not contain as much information as the correlation maps, the line drawing is useful for overlay on other maps and for delineating subtle through-going trends not obvious on other displays. All digital data, together with a descriptive report are available (Gettings and Bultman, 2005).

2. Geologic Setting

The geologic environment of the southwest Colorado Plateau is a thick section of sedimentary rocks (1–3 km) overlying a heterogeneous crystalline basement of contrasting units of magnetization and density. Figure 2 shows a simplified geologic map of the area and several excellent summaries of the geologic history are available (Dickinson, 1989; Beus and Morales, 1990). Here we summarize only the parts of the geologic history of the study area relevant the development of tectonic fabrics and to the hypothesis that surficial fractures vertically correlated with basement lineaments are probably penetrative fractures.

The basement surface is a low-relief erosional peneplain comprised of the 1700 Ma-old Vishnu complex of high grade amphibolitic schists and migmatites with near vertical foliation (Babcock, 1990). These rocks are pervasively
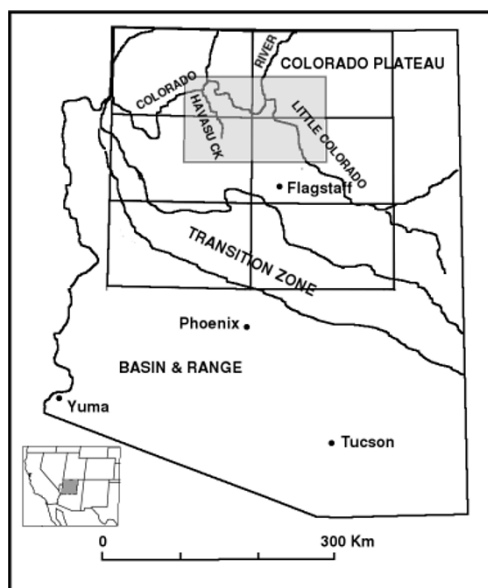
Fig. 1.   Location map showing the locations of the six 1:250,000 scale quadrangles in the study area and various physiographic features mentioned in the text. Quadrangles from top to bottom are Grand Canyon, Williams, and Prescott for the west (left) column and Marble Canyon, Flagstaff, and Holbrook for the east (right) column. Focus area is the lightly gray shaded quadrangle including a quarter each of Grand Canyon, Marble Canyon, Williams, and Flagstaff quadrangles.

intruded with pegmatite dikes and multiple plutonic bodies, mainly granites.   The basement rocks are overlain (Fig. 3) with Precambrian rocks of the Grand Canyon Supergroup (Hendricks and Stevenson, 1990). These rocks contain several disconformities and are block-faulted and tilted. Their upper surface is another low-relief angular unconformity that is overlain by the thick Paleozoic sedimentary section (Huntoon, 1990). These are overlain in turn by Mesozoic and Cenozoic rocks (Morales, 1990) within the study area, although not along the edges of the Grand Canyon. Study of the geologic record (Dickinson, 1989; Hendricks and Stevenson, 1990; Sears, 1990; Morales, 1990; Huntoon, 1990; Ford, 1990) within the study area reveals at least 22 separate episodes of either uplift or subsidence spanning the 1700 Ma of geologic history of the area. At least four of these episodes post-date the youngest Cenozoic sedimentary rocks and thus would have affected the entire stratigraphic section. Huntoon (1990; also, Dickinson, 1989) documents numerous recurrent displacements on Precambrian faults and folds indicating that old zones of weakness successively propagated up section throughout time. We have concluded from this evidence that in most cases, any fault or fracture in the basement will have had some motion along it during the many episodes of uplift/subsidence and
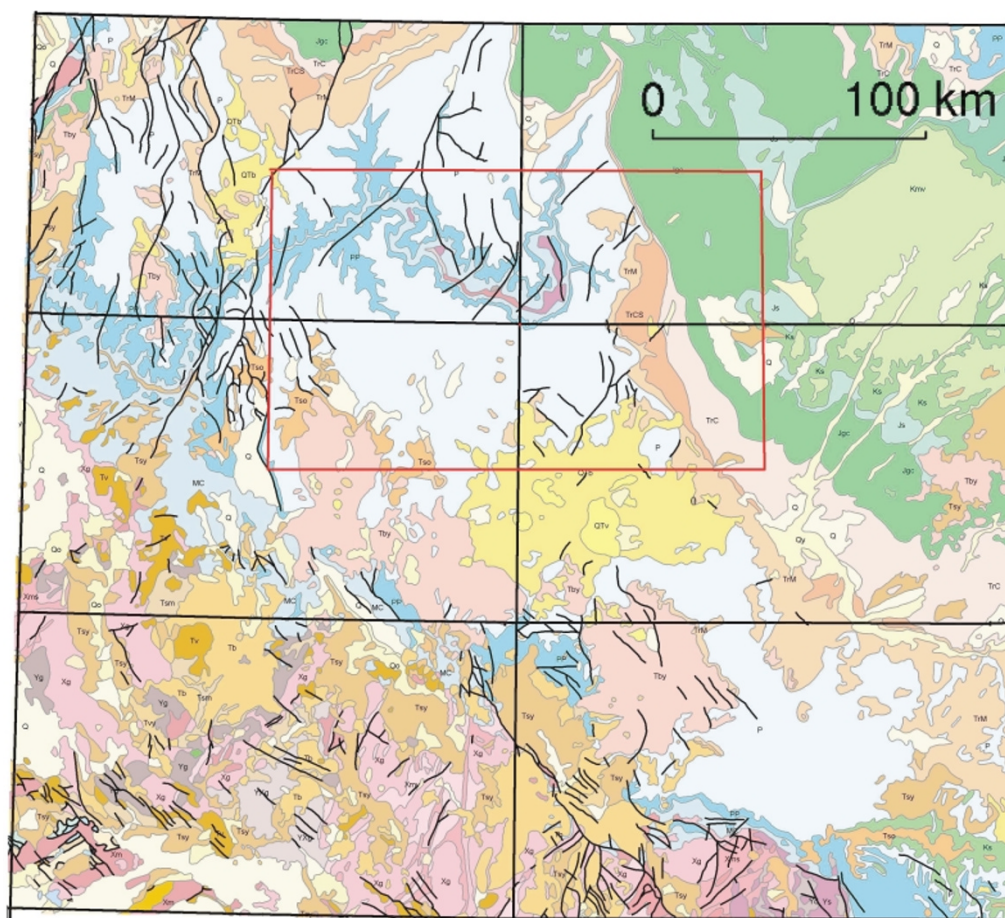

Fig. 2. Geologic map of the study area extracted from Richard *et al.* (2000), showing generalized geologic relations. Pink, purple, and gray colors are Precambrian metamorphic basement rocks, blues represent Paleozoic rocks, and browns and greens Mesozoic rocks. Yellow and salmon colors are Cenozoic volcanic and sedimentary rocks. Faults are shown in bold black, the boundaries of the six quadrangles of the study area are shown in black, and the boundary of the focus area is shown in red. Upper left corner is at latitude 37°N, logitude 114°W; lower right corner is latitude 34°N, longitude 110°W.
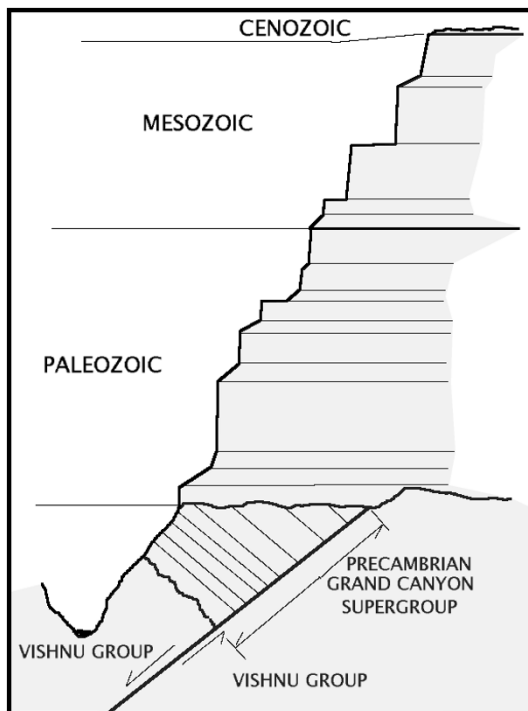
Fig. 3. Cartoon cross section showing the generalized stratigraphic section in the study area. On the diagrammatic edge of the section, more vertical edges represent dominantly cliff-forming sandstone and limestone, and sloping edges represent slope-forming shale and mudstone. The Vishnu Group is metamorphic basement rock. Vertical thickness of the section is about 2,400 m.
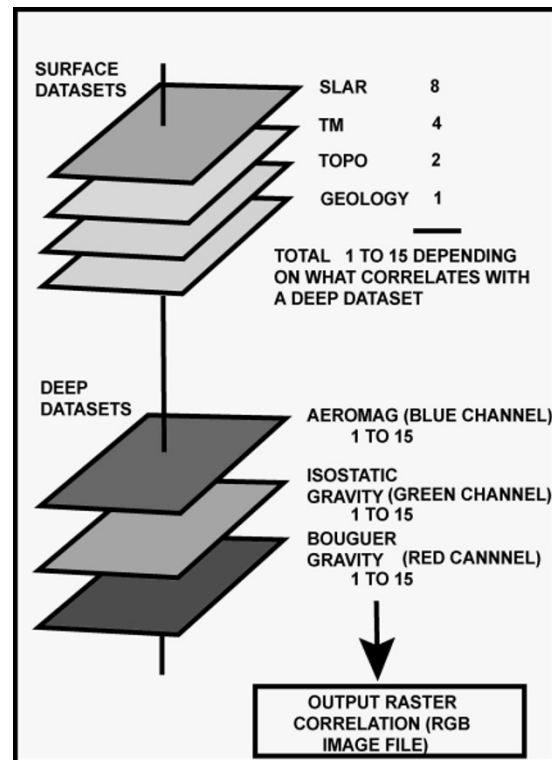

Fig. 4. Schematic diagram of the correlation scheme used to uniquely define correlations between surface and deep lineament datasets. Pixel values of 0–15 are stored in image format in each of the 3 (red, green, and blue) channels, defining all 4096 possible correlations.

thus will likely be a site of penetrative fracturing.

Several orogenic cycles affected the study area during its geologic history (Dickinson, 1989; Huntoon, 1990; Sears, 1990). These compressional events and the subsequent extensional events generated the fracture system trends that are observed today. During late Precambrian, crustal contraction resulted in the formation of northeast trending reverse faults and monoclines; these events were followed by an episode of extension that generated northwest trending normal faults of large displacement (Sears, 1990). The Devonian-Mississippian Antler and Sonoma orogenies were compressional along a west-northwest direction, resulting in north- to north northeast-trending fault and fracture systems. Compression during the Pennsylvanian-Early Permian times was to the northwest and generated northeast-trending fault and fracture systems. Many northeast trending structures were generated or reactivated by the east to southeast compression of the Sevier Orogeny. Within the study area, the Late Cretaceous-Tertiary Laramide orogeny produced compression along northeast to southeast axes to generate or reactivate northwest to northeast faults and fractures. Mid-Tertiary extension along a northeast direction reactivated or generated many northwest-trending structures. Finally, late Tertiary east-west extension has reactivated many north-south trending structural elements (Huntoon, 1990). All of the authors cited emphasize the repeated reactivation of existing structures by subsequent tectonic events. For example, several movements of both a reverse and a normal sense can be demonstrated on the Bright Angel fault (Sears, 1990;

Huntoon, 1990). As will be seen below, the major structural trends described here are well displayed in the trends of the potential field data.

3. Method

In many areas characterized by a thick surficial layer of sedimentary rocks, the mapping of deep penetrative fractures has become an important undertaking. Approximately flat-lying sedimentary sequences often comprise significant portions of basins and plateaus, and if they contain regional aquitards such as shales, mudstones, siltstones, or some limestones, the vertical hydraulic conductivity is essentially zero except where broken by steeply dipping fractures. In these environments, the only significant recharge to deep aquifers is via deep penetrative fractures, and mapping their probable location is thus an important objective for groundwater studies.

Price (1966, 1974; see also Hancock, 1969 and Jaeger and Cook, 1976) showed that large sedimentary basins will develop penetrative joint and fault systems without external deformation due to the stresses involved during downwarp, lithification, and subsequent uplift. Of course, existing stress fields due to tectonic forces will superpose on the basinal stresses and modify the overall stress field and consequent fracture pattern. Thus, most authors feel that fracturing from jointing as well as faulting will generally be penetrative throughout the entire sedimentary section as it exists at the time of fracture development. On the other hand, the nature of the fracturing, that is, whether fractures tend to be single and through going, or branching networks,

Table 1. Summary of the various datasets used in this study.

Dataset	Date acquired	Grid interval, m, or scale	Estimated horizontal accuracy ± m	Reference
Aeromagnetic anomaly	1947–1982	500	250	Sweeney and Hill (2001)
Bouguer gravity anomaly	1930s–2000	500	250	Sweeney and Hill (2001)
Isostatic gravity anomaly	1930s–2000	500	250	Sweeney and Hill (2001)
Geologic mapping	1983–2000	1:1,000,000 (1993, 2000)	500	Arizona Geological Survey (1993);
		1:500,000 (1983)	250	Billingsley (2000); Hirschberg and Pitts (2000);
		1:100,000 (2000)	50	Richard *et al.* (2000)
Digital Elevation Models	1996	30	15	EROS Data Center (2001); USGS (2004)
Side Looking Airborne Radar	1983	25	13	EROS Data Center (2001);
LANDSAT Thematic Mapper	1999	15	8	ARIA (1998)

depends upon both the lithologic character and the tectonic history, as does whether or not the fractures remain open or are closed. For example, a sedimentary section in an extensional stress regime is more likely to have a higher proportion of open fractures than a section in a compressional stress regime. Odling *et al.* (1999) give an excellent review of fracture systems in sedimentary rock sections and their resulting permeabilities for fluid flow in fractures. This study does not address the question of openness of fractures other than to note that the overall stress regime in the study area has been extensional for much of Tertiary and Quaternary time (Huntoon, 1990). The fundamental assumption for this study was that if a surficial fracture correlated downdip with a lineament in the basement rocks, it is probable that it is a penetrative fracture. Thus, the strategy was to map lineaments in the basement that are horizontally curvilinearly persistent, and to superimpose this map on a surficial fracture map derived from geologic and other shallow data.

These assumptions are validated by direct observation in the Grand Canyon area, where the existence of faults and fractures intersecting the canyon walls on the surface of the sedimentary Plateau surface can be directly traced down the canyon wall into structures in the underlying metamorphic and igneous rocks of the basement. The Bright Angel fault zone (Huntoon, 1990), for example, can be observed to offset both the sedimentary and basement rocks. Most side canyons and changes in river course direction in the area are seen to be related to differential weathering along penetrative fractures (Potochnik and Reynolds, 1990; Sears, 1990). Huntoon (1990) points out that virtually all the structures observed in the walls of the Grand Canyon predate the Colorado River and its canyon. Hereford and Huntoon (1990) review several mechanisms of mass wasting occurring from processes related to unloading of the canyon walls from the erosional cutting of the canyon. These processes produce fractures and failure parallel to the walls of the canyon and are not a significant component of the surficial lineament data of this study. The basement crystalline rocks are highly deformed amphibolitic schists with numerous injections of

granitic bodies (Babcock, 1990). The schists are relatively magnetic and dense compared to the granitic zones. The lithologic contacts are steeply dipping to vertical and have strong physical property differences, so that the basement is ideal for producing contrasting signatures in the geophysical data.

There are several sources of errors with the method. For the deep fracture pattern, a lack of sufficiently precise or closely spaced magnetic and gravity anomaly data will mean that not all anomalies will be detected and thus lineaments, especially subtle ones, will be lost. If fracture or fault systems do not juxtapose rocks with contrasting density or magnetization, there will be no anomaly. For the shallow fracture dataset, lack of sufficiently precise data is a limitation, and some man-made features (e.g. roads, pipelines, transmission lines, and railroad tracks) may lead to false identifications. Shallow burial by surficial deposits may obscure fractures. The net result of these sources of error is that the set of penetrative fractures defined by this method is a lower bound on the total set.

4.   Data Compilation and Sources
4.1   Geophysical data

Existing Arizona state complete Bouguer gravity anomaly, isostatic gravity anomaly, and aeromagnetic anomaly data (Sweeney and Hill, 2001) were used for this study. These data are in the form of regular grids with a value at 500 m intervals. The grid interval constitutes a low pass filter on the data so that the precise location of anomaly features cannot be determined at distances less than about one half a grid interval. This fact determined that the scale of the correlation analysis would be 1:250,000 scale. Moreover, in some parts of the study area, the density of observed gravity and/or aeromagnetic data is too sparse to justify interpretation at higher resolution.

4.2   Surficial data

Four types of Earth's surface data were used to detect curvilinear features (lineaments) expressed at the Earth's surface. These were: 1) USGS side-looking airborne radar (SLAR); 2) Landsat 7 Thematic Mapper panchromatic im-

agery (TM); 3) USGS digital elevation models (DEM), and 4) published geologic mapping (Arizona Geological Survey and Bureau of Land Management, 1993; Billingsley, 2000; Hirschberg and Pitts, 2000; Richard *et al.*, 2000). SLAR and DEM data were purchased from EROS Data Center (2001), and TM imagery was obtained from the University of Arizona image archive ARIA (1998). Table 1 summarizes the datasets we used in this study together with their dates of acquisition, resolution, and accuracy.

5.   Geophysical Data Processing

The primary tool for this interpretation was the location of local horizontal gradient maxima (Blakely and Simpson, 1986). These authors show that for relatively steeply dipping to vertical contacts between rocks of differing magnetic and/or density properties, the maximum horizontal gradient in the magnetic (using the "reduction to the pole transformation" or the "pseudogravity transformation") or gravity anomaly field will occur very nearly vertically over the contact between the two differing rock types. Analytic signal maxima (Nabighian, 1972) have been utilized in this study as an additional structural indicator and a means of defining dip of deep structures. If the deep structure has dipping boundaries that are not steep, the horizontal gradient maxima will be displaced downdip from the analytic signal maxima, thus allowing an estimate of the dip. If magnetic horizons are present within the sedimentary section and if there is evidence of significant non-vertical dip of fracture systems, an intermediate depth layer must be utilized. No such horizons were required in this study.

The three geophysical datasets were first subsetted into grids covering each of the six 1:250,000 scale quadrangles of the study area. An arbitrary overlap of several rows and columns outside the actual quadrangle boundaries was included in the grids to insure that there would not be any discontinuities in resolved trends between quadrangles. For each quadrangle, the aeromagnetic data were transformed from dipolar to monopolar form using the "reduction to the pole" transformation (see, for example, Blakely, 1995). This transformation is necessary to prevent distortion of the structural trends mapped by the aeromagnetic anomaly at locations other than the magnetic poles due to the dipole form of magnetic anomalies. Shaded relief images of the aeromagnetic anomaly (not reduced to the pole in order not to distort anomalies in areas with strong remnant magnetization), Bouguer gravity anomaly and Isostatic gravity anomaly were prepared, illuminated from the northeast and northwest respectively, for a total of six maps. These maps allow visual checks of the validity of the trend lines generated by computer. Additionally, they are valuable in the study of the various areas as an overlay to geologic and geographic map data. For each of the three grids (aeromagnetic anomaly reduced to the pole, Bouguer gravity anomaly and isostatic gravity anomaly), the maxima of horizontal gradient and analytic signal were calculated and stored as a set of x,y points locating the maxima on the map. All map manipulation and analysis was done using Oasis Montaj software produced by Geosoft, Inc., Toronto, Ontario, Canada, supplemented with several GX plugins produced by USGS (J. Phillips, written communication, 2003). The use of trade names for software here is for information only and does not constitute an endorsement of the software.

A trend analysis for the three anomaly grids for each quadrangle was performed on the horizontal gradient grid. Because every anomaly is finite in spatial extent, its trends completely encircle it, but any elongation or preferred orientation will show up as a peak above the uniform background in the distribution of trends if a uniform spatial sample is observed. The grid itself is a uniform spatial sample, so by plotting a histogram or rose diagram of the strike of the horizontal gradient at each grid point, an unbiased sample is obtained. Peaks in this distribution represent the trend directions of non-circular anomalies and map the directions of boundaries between various magnetization and density contrasts (Gettings, 2001). This procedure was carried out for horizontal gradient of the reduced-to-pole aeromagnetic anomaly, the Bouguer gravity anomaly, and the isostatic gravity anomaly grids. Grauch (1988) reported similar experiments with gridded data but using average trends within a window moving over the grid.

6.   Surficial Data Processing

Several lineament extraction techniques were applied to each type of surface feature data. The technique chosen for the extraction of lineament features from the data was based on a subjective visual analysis of which method produced the set of lineaments most comparable in linear extent to the geophysical lineaments for each type of data. Lineaments were extracted from the data at the original resolution of the data. All lineament products were interpolated to 30 m pixel size for correlation with geophysical data. Data processing of the surficial imagery datasets was carried out using the image processing software system ENVI produced by Research Systems, Inc. Several programs were written in this system by M. Bultman using IDL (Interactive Display Language) to accomplish the correlations, threshold images, and produce the pixel-encoded RGB correlation images.

Two general problems were encountered in the extraction of curvilinear surface features (surface lineaments) from the data. First, the number of surface lineaments is much higher in areas of canyons, due to the extreme topography, than it is in relatively flat areas. Yet, the lineament extraction method needs to be sensitive enough to identify surface lineaments in both flat terrain and in rugged topography. Because of this, the spatial density of lineaments extracted from the data is much higher in areas with large topographic relief. The second problem is that linear cultural features are extracted from both the SLAR and TM imagery. While this problem was considered in the analysis, it turned out that there are no known cultural lineaments that correlated with geophysical lineaments for distances long enough that they might be considered a significant hydrological structure. In the Holbrook quadrangle, several cases of correlations of aeromagnetic anomaly with surficial lineaments were identified as due to railroad tracks, but the map extent of these correlations is trivial, amounting to less than a kilometer because most of the railroad track does not happen to lie on an aeromagnetic survey flight line.

6.1   SLAR

SLAR radar energy is transmitted perpendicular to the aircraft's flight path. The signal received by the aircraft is a function of the reflectivity and geometry of the objects reflecting the radar back to the aircraft. This signal is processed to produce an amplitude/time video signal with brighter pixels indicating higher energy returns. This creates a series of image strips that are combined into an image of an area. The SLAR images are optically digitized at a pixel size of about 25 meters. Because SLAR illuminates the terrain at an oblique angle, it enhances topographic and geologic features and is therefore ideally suited to the detection of geologically based curvilinear features.

The method chosen for lineament extraction from SLAR data in this analysis calculated the inter-pixel variance within a moving window. A 3×3 pixel moving window was applied to the data and the variance of the 9 pixel values in the window was calculated and assigned to the location of the center pixel. The image of all center pixels produces a new image that maps textures and highlights lineaments (areas where pixel values change rapidly). The variance values in these images ranges from near zero to very large numbers ($>100,000$). The mean variance value within the study area is 300 to 500, but is very dependent on the type of terrain the image encompasses. In order to highlight the important curvilinear features obtained, all values with a variance lower than a chosen minimum value are set to zero and those above are set to one to produce a binary lineament map. In this analysis the minimum variance value was chosen subjectively based on the observed variance distribution in each quadrangle, and varied between 300 and 500 for the six quadrangles.

6.2   Thematic Mapper data

Thematic Mapper multispectral imagery obtained from the Landsat 7 satellite was also used for the detection of curvilinear features on the Earth's surface. This satellite has the latest version multispectral scanner, called the Enhanced Thematic Mapper Plus, referred to as TM here for simplicity. The important component of this new mapper in terms of this analysis is that it is capable of obtaining a panchromatic image with a spatial resolution of 15 m per pixel. This image (TM band 8) provides an increased ability to resolve and detect curvilinear features on the Earth's surface compared to the previous Landsat satellites (NASA, 2004).

The TM data used in this analysis was acquired in early October, 1999. This data should provide good lineament detection in the panchromatic band and also produce good images designed to detect vegetation (Kidwell, 1990). These images are referred to as normalized density of vegetation index (NDVI) images. They are usually computed using two bands from the satellite data, and infrared (IR) and a visible (VI) band. NDVI is then the quotient of the difference over the sum: $(IR-VI)/(IR+VI)$. The vegetation images were used to determine if mapped curvilinear linear geophysical anomaly-surface lineament correlations affect occurrence of vegetation where they intersect canyons.

The method chosen for lineament extraction from TM data was convolution with a directional kernel. This method convolves a 3×3 pixel kernel with the band 8 image. The kernel is designed to enhance features along a specific direction. For this study 4 principal directions were used. These directions are analogous to azimuths of 0, 45, 90, and 135 degrees. Since each convolution results in a separate image with most lineaments running in the direction of the specific kernel direction, the 4 images were added to produce an isotropic lineament image. This lineament image contains a large range of values and a high pass filter was applied to the image to select only important features. All values at or above the minimum for each quadrangle were set equal to one to produce a binary lineament map.

6.3   DEM

Digital elevation model (DEM) data was also used in the Earth's surface curvilinear feature detection. This data numerically represents the topography of Earth's surface and thus includes information on the direct or indirect response of the Earth's surface to geology. The DEM data used here are from the National Elevation Dataset (USGS, 2004) which has a one arc-second (approximately 30 meters) spatial resolution and is the highest resolution dataset available over the entire study area.

The method chosen for lineament extraction from the DEM data was the same method used to detect geophysical anomalies, i.e., the location of local horizontal gradient maxima (Blakely and Simpson, 1986) .

6.4   Geologic mapping

The geologic component of the surface lineament data relies solely on the mapping of faults and folds in geologic maps within the study area. These maps include mapping at 1:1,000,000 scale (Arizona Geologic Survey and Bureau of Land Management, 1993), 1:500,000 scale (Hirschberg and Pitts, 2000), and 1:100,000 scale (in the Grand Canyon 1:100,000 scale quadrangle only) (Billingsley, 2000). Late in the analysis, it was discovered that the 1:1,000,000 geologic map of Richard *et al.* (2000) contained a number of newly mapped faults not present on the 1993 map. These faults were not used in the analysis but were used as a test dataset to evaluate the effectiveness of detection by the method as discussed below.

7.   Correlation of Surficial and Deep Lineament Data

The deep and surficial lineament images were superimposed and candidate penetrative fractures defined by spatial coincidence of features at the pixel (30 m) level using the ENVI image processing software. The geophysical datasets are defined on a much coarser grid of 500 m interval. Because of the larger interval, the precise location of the maximum gradient is uncertain to approximately half the grid interval. However, a property of potential field data requires that the field vary in a smooth and continuous way. This property is utilized in the technique of horizontal gradient location used in this study and generally results in locations more precise than one half a grid unit. As discussed above, the bulk of the geophysical data variations are thought to come from sources in the basement below the sedimentary platform, and in this case the horizontal gradient location is quite precise and of the order of a 100 m or less. If there is significant dip to the surficial fractures, this must be taken into account using depth estimates computed from the grav-
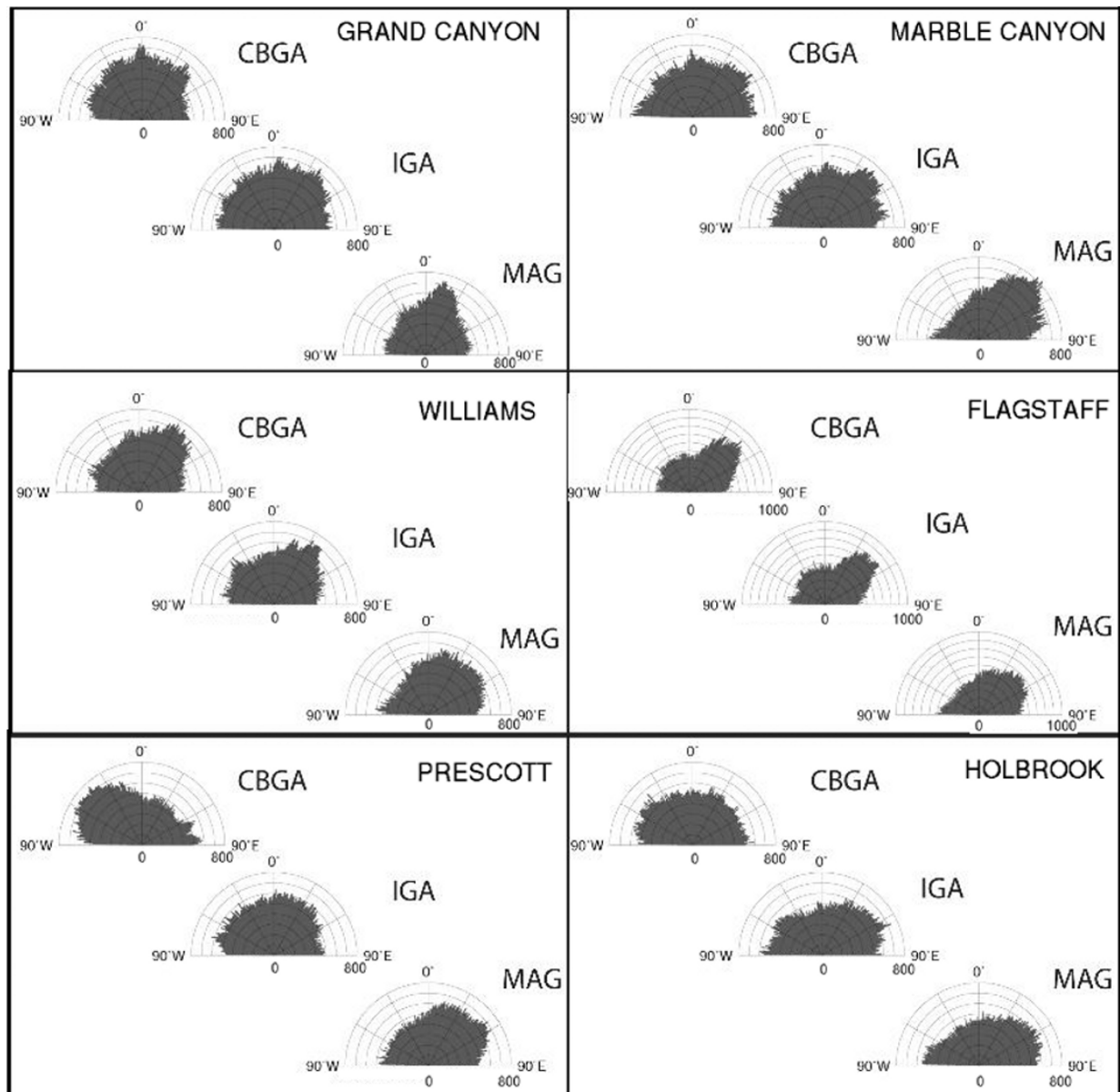
Fig. 5.   Composite rose diagrams for the strike of the horizontal gradient for the complete Bouguer anomaly, the isostatic gravity anomaly and the aeromagnetic anomaly for each of the six 1:250,000 quadrangles of the study area. Quadrangles from top to bottom are Grand Canyon, Williams, and Prescott for the west (left) column and Marble Canyon, Flagstaff, and Holbrook for the east (right) column. Note changes in distribution of trends for the different quadrangles.

ity and magnetic anomaly data. In order to account for the uncertainty of gradient locations due to the geophysical data grid spacing and dip of fractures, we allowed correlations within ±1/2 grid unit (250 m) of a deep lineament. This allows for dips of about 50°–130° between the surface and the deep structure for typical depth to basement of about 1 km, which is representative for the study area.

The three geophysical lineament sets (aeromagnetic, Bouguer gravity anomaly, and isostatic gravity anomaly) correlated spatially with the surficial lineament sets produced a database. The data were stored in the format of an RGB image, with correlations of surficial lineaments with Bouguer gravity anomaly in the red channel, correlations with isostatic gravity anomaly in the green channel, and correlations with aeromagnetic anomaly in the blue channel. One RGB-format database was constructed for each

of the six quadrangles, and one for the focus area. In each database, pixels in each of the three channels with no correlation were set to 0 (black); pixels that correlated with surficial datasets were given nonzero numbers coded to show with which of the surficial datasets the geophysical data were correlated (Fig. 4). In each channel, a correlation with: geology was set to 1; topography was set to 2; thematic mapper was set to 4; and a correlation with SLAR was set to 8. Using this scheme, the sum of the numbers is unique for every combination of correlations so that no information is lost. Thus, the 4096 total possible combinations of correlations for every pixel are stored in three channels as a number between 0 and 15 for every pixel covering the study area with. For example, a value of 7 in the red channel and 0 in the green and blue channels for a pixel means that Bouguer gravity anomaly correlates with geol-

Table 2.   Azimuthal bands of distinctive trends of horizontal gradient for the six quadrangles of the study area. Abbreviations: CBGA—complete Bouguer gravity anomaly; IGA—isostatic gravity anomaly; AMA—aeromagnetic anomaly. Numbers in parentheses give the subjective relative rank of the peak in the trend distribution, for example, (1) is a first order or dominant trend, (2) is second order, and so on.

Quadrangle	CBGA	IGA	AMA
Grand Canyon	(1) 350–005	(1) 000–015	(1) 010–025
	(1) 040–045	(1) 035–045	(2) 320–010
	(2) 320–345	(2) 320–345	(2) 040–060
	(2) 005–040	(2) 020–035	
	(3) 280–315	(3) 290–305	
		(3) 250–280	
Marble Canyon	(1) 355–005	(1) 030–060	(1) 040–050
	(1) 050–060	(2) 000–020	(2) 015–040
	(2) 070–100	(2) 065–080	(2) 050–065
	(2) 030–050	(3) 270–320	(3) 070–085
	(3) 310–345	(3) 325–350	(4) 265–290
	(3) 005–030		
Williams	(1) 020–040	(1) 025–040	(1) 010–025
	(2) 345–020	(2) 310–320	(2) 025–065
	(2) 040–050	(2) 015–020	(3) 340–010
	(3) 290–345	(3) 040–070	(3) 275–285
		(3) 280–310	
		(3) 340–015	
Flagstaff	(1) 040–050	(1) 040–045	(1) 035–055
	(2) 025–035	(1) 050–055	(2) 355–035
	(2) 050–060	(2) 020–035	(2) 055–070
	(3) 310–355	(2) 055–070	(3) 270–290
		(3) 275–285	
		(3) 300–015	
Prescott	(1) 275–340	(1) 000–045	(1) 045–070
	(2) 015–040	(2) 285–000	(2) 005–045
	(2) 065–070	(3) 050–065	
	(2) 080–090		
Holbrook	(1) 300–320	(1) 060–070	(1) 040–080
	(2) 280–290	(2) 265–280	(2) 005–040
	(2) 015–035	(2) 020–060	(2) 265–290
		(2) 070–080	
		(3) 300–320	
		(3) 350–000	

ogy, topography, and thematic mapper, and isostatic gravity and aeromagnetic anomalies do not correlate. Although the database cannot be displayed as a meaningful image, by loading the database into the image processing software one can examine pixel-by-pixel the correlation values to determine which surficial data layers correlated with geophysical layers.

8.   Results

The various datasets and their supporting metadata discussed above, together with the derivative overlay images produced a data archive of more than 80 Gigabytes (Gettings and Bultman, 2005). Most layers are stored in Geotiff geographically registered image format or in appropriate files for import into the ARC/INFO Geographic Information System. In particular, in addition to the image-format version, the three layers are also given as ARC Grids for each of the six quadrangles and the focus area giving the final correlations coded from 0–15 for each 30 m pixel as discussed above. These grids are called the correlation maps and constitute the final products of this analysis; they map the locations of candidate deep penetrative fractures for the study area. We have not been able to find any satisfactory way of displaying the total information content of these grids to date, however we have summarized the grids in several ways described below. The archive also contains all supporting data used in the analysis and several visualizations and summaries of the correlations.

The trend analysis of the three geophysical grids was prepared as a set of eighteen rose diagrams, one for each quadrangle for each of the three geophysical grids. These diagrams have been combined into a single diagram in Fig. 5

with the rose diagrams plotted in the map position of the quadrangle to which they apply. This enables comparison of the diagrams with the geologic map of Fig. 2. Table 2 lists the ranked trend set directions determined by the authors from study of Fig. 5 for these diagrams for each anomaly type and each quadrangle.

Correlation NDVI maps were produced for the six quadrangles and focus area in order to determine if there was any relationship between correlations and surface vegetation. These images are geotiff images of the normalized difference vegetation index with all correlations overlain. The correlations are not keyed to either geophysical data or surface lineament data, but are all presented as one color to make the map as readable as possible. Relationships to geographic features were studied by overlaying correlations on Digital Raster Graphic (DRG) maps. A special coding was used for the correlations in this map, since the 4096 different possible correlations would create a map that was very difficult to read. Correlations were coded only to the geophysical data, so that where surface lineament data of any kind (SL) correlated only to complete Bouguer anomaly data (CBA), the correlations were presented in red; where SL correlated only to isostatic gravity anomaly data (IGA), the correlations were presented in green; and where SL correlated only to aeromagnetic anomaly (MAG) data, the correlations were presented in blue. The following combinations of correlations were also shown. SL correlated to CBA and IGA was shown in yellow, SL correlated to CBA and MAG was shown in magenta, SL correlated to IGA and MAG was shown in cyan, and SL correlated to CBA, IGA and MAG was shown in black. Pixels with zero correlation were set to white. Figure 6(a) shows a histogram of the correlations in this coding scheme for the focus area. Geophysical lineaments in approximately 1.7 million of the 22.6 million pixels in the focus area correlated with one or more surfaces lineaments, or about 7.5% of the focus area has correlations. About 2.9% correlate SL with gravity lineaments and about 3.5% of the correlations are with aeromagnetic lineaments. Only about 1% of the total pixels correlate with both aeromagnetic and gravity lineaments. The stronger correlation with aeromagnetic lineaments is to be expected for two reasons. First, the aeromagnetic data coverage is denser than that of the gravity data and thus resolves more lineaments, and second, the gravity anomalies reflect deeper structures in the basement in addition to the shallow basement, whereas the the aeromagnetic lineaments reflect primarily shallow basement structures. Within the correlations, about 40% are with gravity lineaments and about 60% are with aeromagnetic lineaments.

Figure 6(b) shows how the surface lineaments correlated with the geophysical lineaments for the focus area. The shapes of the distributions for the three geophysical datasets are similar, with the two gravity anomaly lineament correlations being virtually identical. Aeromagnetic lineament correlations are more numerous in all categories except correlation with all four surficial lineament datasets. For single dataset correlations, SLAR correlations are most common, followed by TM, topography, and geology. The smaller correlation with geology may in part be due to the fact that the fault and fold trace dataset is the smallest of the surficial lin-
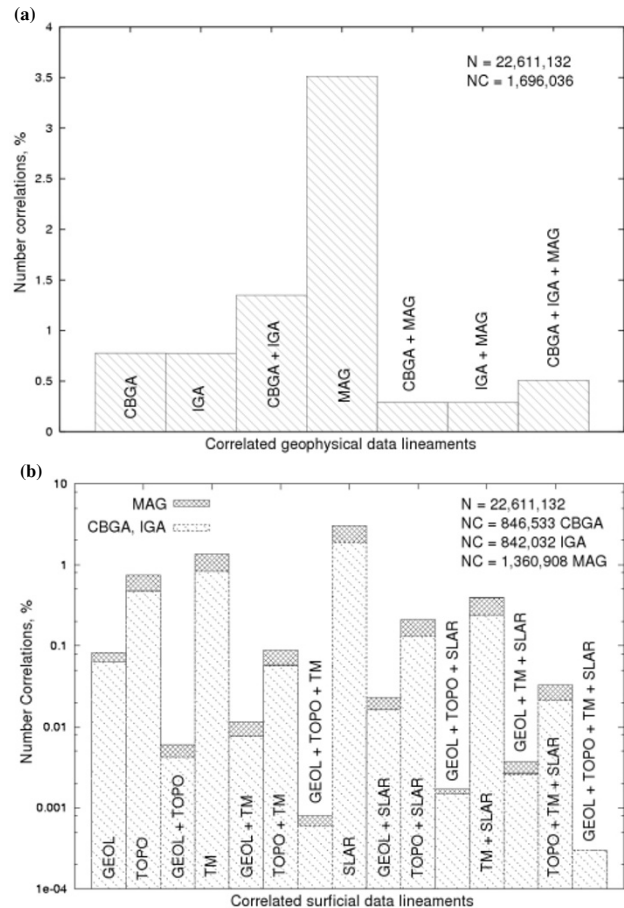

Fig. 6. Histograms of correlations for the focus area. (a) Correlations of one or more surficial lineament datasets with geophysical lineament datasets (CBGA, complete Bouguer gravity anomaly; IGA, isostatic gravity anomaly; MAG, aeromagnetic anomaly). N is the total number of pixels in the focus area, including correlation and no correlation pixels; NC is the total number of focus area pixels with correlation. (b) Correlations of geophysical lineament datasets with combinations of the four surficial lineament datasets, abbreviations as in a), and GEOL, geologic maps; TOPO, digital elevation models; TM, LANDSAT Thematic Mapper; and SLAR, side looking airborne radar. Note logarithmic scale for the number of correlations in percent and that the distributions are nearly identical in shape with larger values for the aeromagnetic anomaly correlations.

eament datasets. Single dataset correlations are generally much more numerous than correlations with several surficial datasets. For the multiple correlation cases, TM and SLAR and topography and SLAR are the most numerous, and correlation with all four surficial datasets is least frequent.

Finally, in the focus area, a line drawing map (see Fig. 7 for a portion) was prepared by drawing lines by hand on an overlay of a color plot of the seven-color correlations described above. This image contains much less information than the correlation maps since it only shows presence or absence of correlation; it is nevertheless useful in the detection of through-going lineaments and as an overlay on geologic maps. A disadvantage of this map was that it required a long time to prepare (about 100 hours), although using image processing techniques, the authors believe preparation time could be reduced significantly.
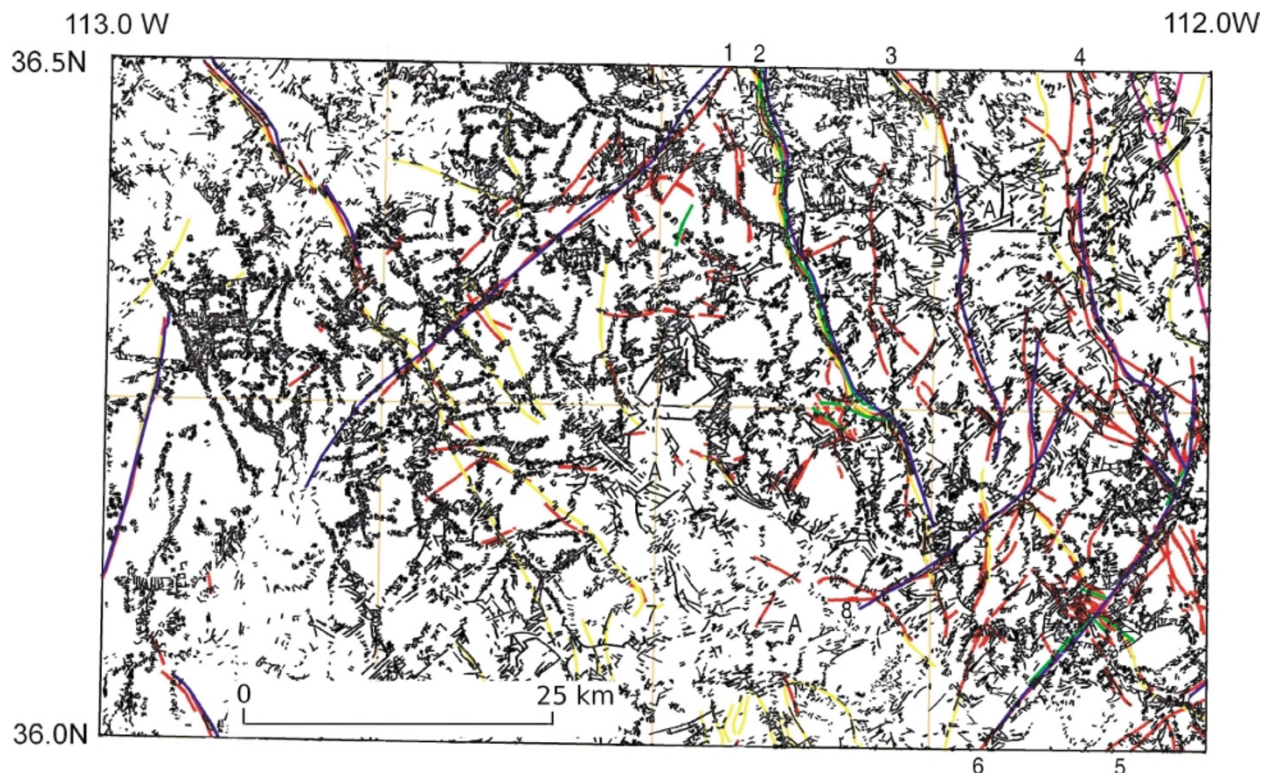
Fig. 7. Northwest quarter of the line drawing of correlations between deep- and shallow-lineament datasets for the focus area (see Figs. 1 and 2 for focus area location). Colored lines are from geologic maps: red, green and blue lines are faults; and yellow and magenta lines are fold axes. Thin orange lines are 15′ latitude-longitude grid lines. Labeled features are; 1, Sinyala fault; 2, Crazy Jug monocline and Muav fault; 3, Big Springs fault and monocline; 4, Uncle Jim fault; 5, Vishnu and McKee faults; 6, Bright Angel fault; 7, Supai monocline; and 8, Slate fault. Labels "A" show examples of parallel lineaments ("railroad tracks") from analytic signal and horizontal gradient that indicate more shallow dip in the basement contacts.

9. Discussion

We were surprised at the large number of correlations and how well the method seemed to work. The method is almost completely carried out by computer and requires a minimal number of subjective decisions, namely decisions that produce surficial lineament densities comparable to those from the geophysical data. This makes the approach quite objective and repeatable because the actual delineation of lineaments is not carried out by a subjective process.

Close examination of the line drawing (Fig. 7) shows that there are several kinds of correlation: correlation of deep lineaments with surficial faults, folds or lineaments that result in a line, and correlation with surficial joint patterns that result in en echelon patterns or paths of joint-like correlation because of the "smearing" of the deep lineament location to account for the low-pass filter effect of the gridding of the geophysical data and possible dip of structures. As discussed above, joints are generally thought to be penetrative as well as faults, so that correlations with surficial joints are as important as correlations with faults and there is no reason to expect that existing joints, when favorably oriented, would not accommodate offset. Figure 7 shows examples of both correlations together with "railroad track correlations" that occur for two reasons. First, small offsets occur because of location discrepancies of fold axes and fault traces between the various geologic map datasets from differences in scale and accuracy of compilation. Second, and more importantly, if a boundary in the geophysical datasets is not dipping steeply, the horizontal gradient max-

ima will be displaced downdip from that of the analytic signal. This results in correlations with two parallel lines (see locations labeled "A" in Fig. 7), and thus show where dipping basement structures may be important. Labeled faults and fold axes on Fig. 7 show that while most mapped faults are detected at least in part, fold axes are much less frequently mapped and often have no geophysical expression.

For areas outside of the focus area, the correlations images in their various forms can be used instead of the line drawing. The line drawing is in fact a very simplified version of the correlations, and the 0–7 coded geophysical lineaments correlations, or some version of the full correlation grids, should be used instead. This would permit the application of correlation rules such as correlations from several datasets being more heavily weighted than only one correlation. The line drawing does have one advantage, which is to highlight some penetrative structures that can be traced across the entire area, sometimes as fault/fold axes and elsewhere utilizing joints for some portion of the lineament. Several such features can be seen on Fig. 7, especially eastnortheast directions and north-south directions.

The large number of correlations additional to those defined in surface geologic mapping leads one to the question of whether the correlations are real or fortuitous. A contact in the basement between two contrasting rock types should not necessarily lead to offset and penetrative fracture. We have concluded, however, that most if not all of the correlations are probably real for the following reasons. First, the geologic history, reviewed briefly above, docu-

ments numerous episodes of uplift, erosion (presumably differential depending on lithology and degree of fracturing), subsidence, sedimentation, lithification, compression, and extension. With such a long history of repeated tectonic stress, it seems to us that virtually every fracture, zone of weakness, and even many contacts (surfaces of differing rock strengths) have probably moved in response. Second, our correlation maps compare well with known tectonic features (see, for example, Sumner, 1985), especially fault zones, or are parallel with or strike extensions of known features. Third, late in this study we discovered that the geologic map of Richard *et al.* (2000) contained a substantial number of previously unmapped faults not present on the maps we used in the analysis. Within the focus area, there are about 50 new faults (depending on how one counts segments following the same strike) shown on this map. Of these 50, only three short segments were not detected at least in part by our correlations. Figure 8 shows an example containing two of the undetected fault segments. In general though, we find that most faults have correlations only in segments, rather than in long continuous lines, and quite a few (perhaps 10–15%) do not have a geophysical expression and thus no correlation. The analysis also suggests that many of the mapped faults have extensions not mapped on the surface and in some cases, nearby parallel structures.

If the correlations or a subset of them are fortuitous, then in such a large study area they should show a near random distribution, since correlations would not be connected by penetrative fractures. Correlations would occur where the (numerous) surficial fractures happened to lie above a basement rock physical property contrast. In order to test if the distribution of correlations was random, we employed quadrat analysis (Thomas and Huggett, 1980). This technique was applied to the Grand Canyon 1×2 degree quadrangle in order to study the spatial distribution of all correlations generated between the geophysical anomaly data and the surface lineament data. The Grand Canyon quadrangle was chosen because it had the most numerous and visually the most random distribution of correlations. The analysis was applied to a 174 km by 108 km portion of the quadrangle; only a small area along the borders was omitted in order to use quadrats that contained exactly 100 rows and 100 columns in the 30 m pixel size correlation image, that is, 3 km by 3 km quadrats. This produced 2088 quadrats. The smallest number of correlations in a quadrat was 11 the largest was 4420. The variance/mean ratio (Thomas and Huggett, 1980) of all correlations in the 2088 quadrats is 523.3 indicating that the correlations neither follow a uniform (variance/mean ratio of zero) nor a random (variance/mean ratio of unity) spatial distribution in the quadrangle. Such a large ratio indicates that the correlations are non-random and strongly clustered spatially (Thomas and Huggett, 1980).

Figure 5 shows a summary of the rose diagrams for the trends of the three anomalies for each of the six quadrangles. There are significant changes between quadrangles showing that there are variations in the tectonic histories as one moves about the study area. In Table 2 we have ranked the trend directions of the more important trendsets. Comparison of Fig. 5 with Fig. 2 shows that in general the
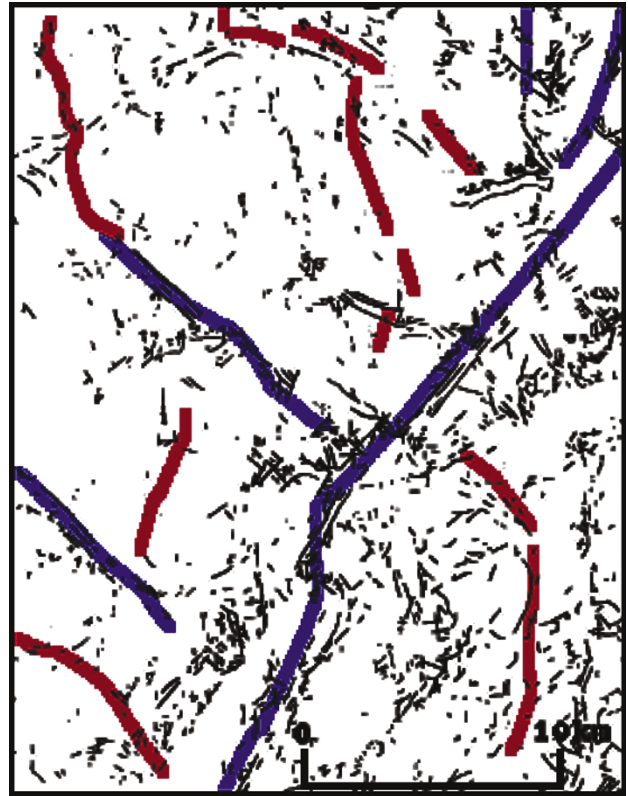

Fig. 8.   Illustration of correlation with faults not present in the geologic dataset. Broad colored lines are centered on faults from geologic maps. Blue faults were present in the database during the analysis, and the red faults were not present. Note that parts of all but two red faults were detected from correlation with other surficial data. Note also parallel trends in black linework ("railroad tracks") indicating non-vertical dip in the basement sources causing geophysical lineaments.

peaks in the trends on the rose diagrams correspond to the directions of faults for the first and second order trendset directions. All of the trendset directions correspond to fracture directions defined from the various orogenic and extensional cycles of the geologic history discussed above, and are for the most part identical with major trend directions described by Blank *et al.* (1997) for the northern Colorado Plateau.

Two systematic relations in peak positions are present in Fig. 5. First, there is a counter-clockwise movement of the peaks of 5–15 degrees observed for each data type as one proceeds westward and to a lesser degree, southward. Blank *et al.* (1997) show that the center of arcuate structures defined by gravity and aeromagnetic data in the northern half of the Colorado Plateau is southwest of the Four Corners area, near the central eastern edge of the Marble Canyon quadrangle (Fig. 2) and point out this is approximately the center of the topographic uplift of the plateau. We observe similar arcuate anomalies in a zone along the margin of the Colorado Plateau to the west and southwest in the gravity and magnetic anomalies. The counter-clockwise movement of trend peaks in Fig. 5 as one approaches the west and southwest margins of the plateau thus probably represents the superposition of structures parallel to the plateau margin on the regional structures defined in the central part of the Colorado Plateau.
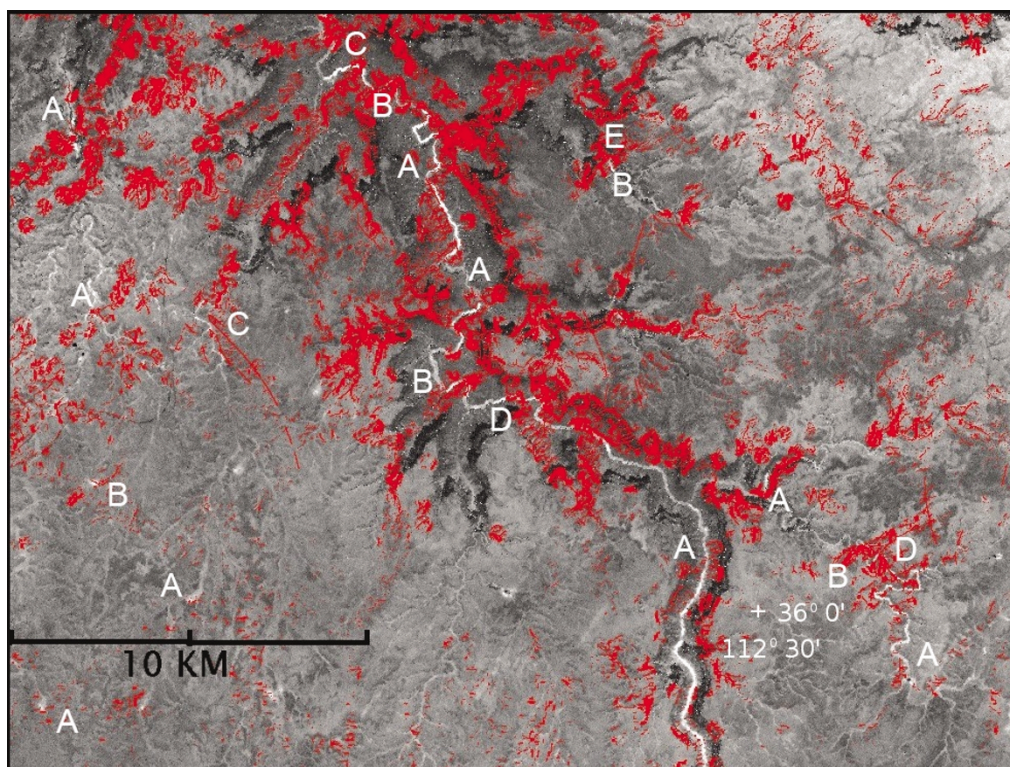
Fig. 9. Normalized Density of Vegetation Image of the Havasu Creek area just south of its confluence with the Colorado River. Red overlay is the deep geophysical-shallow surficial lineament correlation dataset. Letters mark a sample of points where a nearby intersection of a red trend with the drainage changes the NDVI in the drainage, signifying a change in the amount of vegetation and by implication the amount of available nearsurface water. A is an east-west trend; B, northeast-southwest; C, northwest-southeast; D, north-south; and E, combination of trends. All trend directions are approximate.

Where one can correlate peaks in the rose diagrams for aeromagnetic, isostatic gravity, and complete Bouguer gravity anomalies, there is a clockwise movement of the trendset peak from Bouguer gravity anomaly to isostatic gravity anomaly to aeromagnetic anomaly of 5–10 degrees between each dataset. The Bouguer gravity anomalies should reflect sources ranging in depth from shallow crustal structures to deep structures in the mantle, whereas the isostatic gravity anomaly generally are attributed to structures at crustal depths, and the aeromagnetic anomalies generally attributed to sources in the upper crust. The trendsets from the three datasets thus show trends coming from different depths, and combinations of the three rose diagrams should be able to define trends coming from deep, intermediate, and shallow structures. The trendset peak locations of this study (Fig. 5) show that the trends from inferred shallow structures (aeromagnetic data) are typically 10–20 degrees clockwise from the trends inferred to come from the deepest structures (Bouguer gravity anomaly). We are unsure of the cause of these trendset differences, but they may be due to upper Mantle and lower crustal structures from the low angle subduction beneath the western Cordillera postulated by many authors (reviewed in Blank *et al.*, 1997).

Sumner (1985) has described the structural features observed in the gravity and aeromagnetic anomalies of the study area as part of his interpretation for the entire state of Arizona. His work described the regional scale fault zones, large structures and crustal igneous events observable in the potential field data, and provided a basis for our more de-

tailed interpretations within the study area. The Prescott quadrangle in the southwest study area shows a strong peak in the northwest direction (Fig. 5) corresponding to the large scale northwest trending structures of the Transition Zone from the Colorado Plateau to the Basin and Range provinces. In this quadrangle the aeromagnetic and isostatic gravity trends are strongly northeast, corresponding to the smaller structures and lithologies that have a strong northeast trend in the Prescott area. The Grand Canyon quadrangle shows dominantly north-south and northeast trends as well as lesser northwest and east-west trend sets. The eastern column of quadrangles (mostly well within the Colorado Plateau) shows dominantly northeast trends, but with large differences between Marble Canyon and the two quadrangles to the south, as one moves south and away from the center of the Plateau. Marble Canyon also has strong sets of lineaments trending north-south, northwest, and east-west. It is notable that although most of the quadrangles show strong northeast and northwest lineaments, all quadrangles contain subsets of approximately north-south and east-west lineaments. The Williams quadrangle has similar trends to the those of Flagstaff plus a superposed set of trends representing structures parallel to the Plateau edge. Figure 5 contains a great deal of information related to the tectonic history of the southwestern Colorado Plateau and deserves further study. Further research in combining the diagrams to obtain filtered datasets of shallow, intermediate, and deep structural trends is needed. Using a moving window over the datasets (similar to that described by Grauch, 1988)

would define continuous variations of the trendsets in a way useful for regional tectonic studies.

Blank *et al.* (1997) have observed a distinct set of structures in a band overlapping the northern Colorado Plateau margins and the surrounding extensional provinces. They suggest that these structures may represent gravitational collapse radially outward from the center of uplifted Plateau, and that there may be magmatic infilling between the blocks of Precambrian basement in this zone of outward extension. We see evidence for the same types of arcuate structures in the geophysical anomalies of the study area along the western and southwestern Plateau margin. Force (1997) has documented 7 km of Eocene magmatic thickening in the Santa Catalina core complex off the south-southwest margin of the Plateau, and Gettings (1996) showed that "rafting" of the Whetstone Mountains by a subsurface Tertiary intrusive was the only simple way to explain the aeromagnetic and gravity anomalies. Gettings (1994) suggested that magmatic infilling between extended basement blocks was a major cause of the regional aeromagnetic and gravity anomalies in southeastern Arizona. These magmatic events are essentially contemporaneous with the timing of uplift of the Plateau (about one km post-Laramide Paleogene uplift and about three km Neogene uplift, reviewed in Blank *et al.*, 1997).

Images showing the derived deep- and shallow-data correlations superimposed on the NDVI images show clearly that many correlated lineaments are controlling surface waters (an example is shown in Fig. 9). We infer that structures corresponding to the correlated lineaments are damming near-surface water or creating springs in drainages so that water is held sufficiently close to the surface to support vegetation, thus producing whiter portions of the drainage. In areas where the structure appears to abruptly cut off the NDVI downstream, we infer that the structure intercepts the drainage and takes the water to deeper depths so that there is little or no vegetation downstream. The controls by east-west lineaments is somewhat surprising as the east-west lineaments were thought to be a fabric in the basement but are not obvious on the surface without the methods of this study. Numerous cases can be seen on Fig. 9 where whiter sections of drainages are bounded by intersecting correlations. On the other hand, there are several areas of vegetation that do not show any control by correlations and thus are apparently not related to deeper structures. The NDVI images also are a convenient means of locating springs and seeps that have substantial associated vegetation within the Grand Canyon.

Assuming that most of the correlations between the geophysical and surficial datasets do indeed represent penetrative fractures, the density or frequency of occurrence of correlations on a per square kilometer basis from the results of this study constitutes a crude estimate of fracture density, and by logical extension, the possibility of hydrologic recharge to deeper levels by flow down fractures. This is visually seen as areas of sparse or dense line occurrence in the line drawing (Fig. 7). Continuous quantitative estimates can be calculated by passing a window over the correlation grids and counting the number of non-zero pixels within the window. Figure 10 illustrates a test case from within the fo-
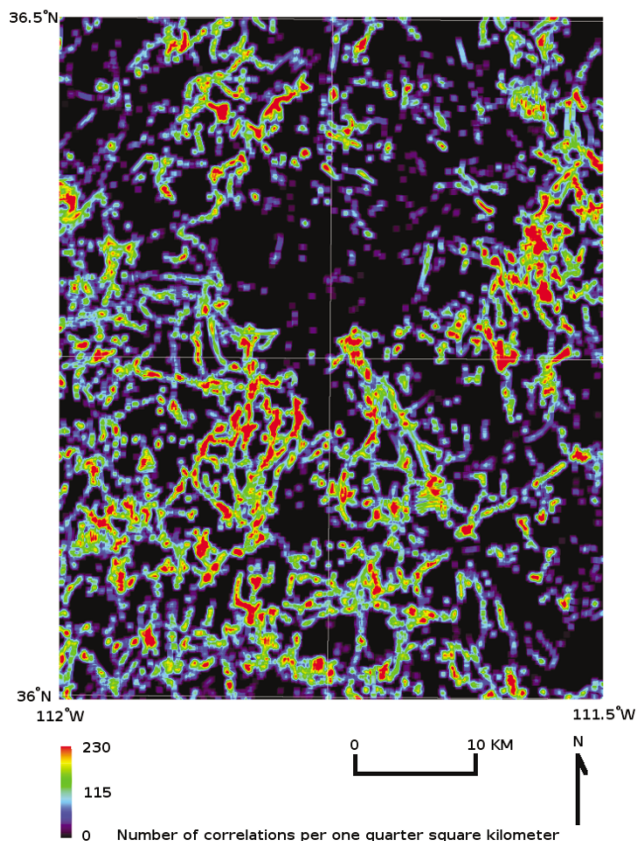

Fig. 10. Spatial density of correlations of all types for a portion of the focus area. Warmer colors represent more correlations per unit area. In the study area environment, areas of higher density of correlations represent candidate areas for more penetrative fracturing and therefore more recharge than areas of low correlation density (for example, dark area in upper center of figure).

cus area and shows clearly the variability of candidate fracture density. By varying the window size in the calculation of the density of correlations, appropriate grids of possible fracturing could be produced for ground water models. Because of the regional scale of the geophysical data used in this study, the data are probably only reliable at a regional ground water model scale with grid intervals of 500 m or greater. Use of these grids for site-scale ground water models might not be reliable because of averaging over only a few (30 m) pixels. In the future, we plan to experiment with imposing different correlation criteria, such as requiring correlation with two or more geophysical datasets or requiring correlation with multiple surficial datasets in order to produce maps with varying criteria for the density estimates.

All correlations were equally weighted in this study. In the future, however, we hope to apply various weighting schemes to emphasize, for example, areas where more than one surficial dataset correlated at depth, or where more than one deep dataset correlated with the shallow lineaments. We intend to investigate using possibility theory (Kandel, 1982) to make logical combinations of all the correlations at each pixel location with the goal of finding the best and poorest correlations according to some selected set of criteria or weighting rules. Analyses such as these can easily be

carried out using the grids that give the pixel-by-pixel correlations for the aeromagnetic, Bouguer gravity and isostatic anomalies.

10.   Conclusion

The methods used in this study objectively and repeatably locate a subset of deep penetrative fracture candidates. They do not, however, provide any information as to whether any fracture is open or closed. In some cases, time domain electrical sounding can detect whether or not a particular fracture is water-filled or not, however there is at present no method to survey large areas such as the area of this study for reasonable costs. It is also to be remembered that if a structure in the basement does not juxtapose rocks of differing density or magnetization, there will be no geophysical anomaly and thus no deep lineament to correlate with surface lineaments. Because of this and lack of detailed spatial data coverage, there are probably many more deep penetrative fractures than mapped by this study. All of the important deep fracture directions detected by this study are accounted for by known tectonic events in the geologic history. This study has, however, mapped many extensions of known structures and delineated numerous new structures parallel to known ones.

The correlation maps produced in this study provide a map of the tectonic fabric for the Southwestern Colorado Plateau and the interpretation of this fabric will be a fruitful area of research. We believe the results presented here point to a complex history of plateau uplift and radial horizontal extension in a broad transition zone around the margins of the Plateau.

The method described here yields a subset of candidates of deep penetrative fractures except for coincidental correlations. We have shown that the distribution of correlations is highly clustered and non-random, and thus most correlations are unlikely to be coincidental. The locations of candidate deep fractures are presented at a resolution (pixel size) of 30 m, but are subject to errors in location of up to plus or minus 250 m due to the 500 m grid interval of the geophysical data defining the location of deep structural boundaries. Numerous new zones of deep fracturing possibility have been defined and are archived in digital grids that uniquely define which deep and shallow datasets correlate. Once threshold parameters are chosen for the lineament extraction algorithms, the procedure is objective and repeatable.

The inferred structures appear to also control near-surface water movement in some cases. The spatial density of correlations (Fig. 10) gives a starting approximation of areas of poor and good recharge possibility due to deep fracture density. Finally, possibility theory from fuzzy logic, or some other schema of criteria, could be used to further quantify and discriminate the correlations.

References

ARIA, Arizona Regional Image Archive, University of Arizona on-line resource, http://aria.arizona.edu/, 1998.

Arizona Geologic Survey and Bureau of Land Management, Arizona geologic map, scale 1:100,000, Arizona Geological Survey Map 26, Arizona Geologic Survey, Tucson, AZ, 1993.

Babcock, R. S., Precambrian crystalline core, in *Grand Canyon Geology*, edited by S. S. Beus and M. Morales, pp. 11–28, Oxford University Press, 1990.

Beus, S. S. and M. Morales, Introducing the Grand Canyon, in *Grand Canyon Geology*, edited by S. S. Beus and M. Morales, Oxford University Press, pp. 1–10, 1990.

Billingsley, G. H., Geologic map of the Grand Canyon 30′ × 60′ quadrangle, Coconino and Mohave Counties, northwestern Arizona, U.S. Geological Survey Geologic Investigations Series I-2688, U.S. Geological Survey, Reston, Virginia, 2000.

Blakely, R. J., *Potential Theory in Gravity and Magnetic Applications*, Cambridge University Press, 441 pp., 1995.

Blakely, R. J. and R. W. Simpson, Approximating edges of source bodies from magnetic or gravity anomalies, *Geophysics*, **51**, 1494–1498, 1986.

Blank, H. R., W. C. Butler, and R. W. Saltus, Neogene uplift and radial collapse of the Colorado Plateau-regional implications of gravity and aeromagnetic data, Laccolith Complexes of Southeastern Utah, Time of Emplacement and Tectonic Setting—Workshop Proceedings, J. C. Friedman and A. C. Huffman, coordinators, *U.S. Geological Survey Bulletin*, **2158**, 9–32, 1997.

Dickinson, W. R., Tectonic setting of Arizona through geologic time, in *Geologic Evolution of Arizona*, edited by J. P. Jenny and S. J. Reynolds, Arizona Geological Society Digest 17, Tucson, Arizona, pp. 1–16, 1989.

EROS Data Center, U.S. Geological Survey, Sioux Falls, South Dakota, http://edc.usgs.gov/, 2001.

Force, E. R., *Geology and Mineral Resources of the Santa Catalina Mountains, Southeastern Arizona: A Cross-Sectional Approach*, University of Arizona Center for Mineral Resource, University of Arizona Press, 135 pp., 1997.

Ford, T. D., Grand Canyon Supergroup: Nankoweap Formation, Chuar Group, and Sixtymile Formation, in *Grand Canyon Geology*, edited by S. S. Beus and M. Morales, pp. 49–70, Oxford University Press, 1990.

Gettings, M. E., Some structural features along the Tucson–Mogollon Corridor inferred from gravity and magnetic anomaly data, USGS Circular 1103-A (Program and abstracts for 1994 McKelvey Forum), pp. 38–39, 1994.

Gettings, M. E., Aeromagnetic, radiometric, and gravity data for Coronado National Forest, in *Mineral resource potential and geology of Coronado National Forest, Southeastern Arizona and Southwestern New Mexico*, edited by E. A. du Bray, *U.S. Geological Survey Bulletin*, **2083-D**, 70–101, 1996.

Gettings, M., An objective method of delineating trends in potential field data: International Association of Geomagnetism and Aeronomy IAGA-IASPEI Joint Assembly Abstracts, August 19–31, 2001, Hanoi, Vietnam, p. 251, 2001.

Gettings, M. E., Identification of possible deep penetrative fractures on the southwestern Colorado Plateau, U.S.A.: International Union of Geodesy and Geophysics XXIII General Assembly, IUGG 2003 Scientific Program and Abstracts, June 30–July 11, 2003, Sapporo, Japan, p. B257, 2003.

Gettings, M. E., A method of delineating deep penetrative fractures in thick sedimentary rock sequences, International Union of Geodesy and Geophysics XXIII General Assembly, IUGG 2003 Scientific Program and Abstracts, June 30–July 11, 2003, Sapporo, Japan, p. B259, 2003a.

Gettings, M. E. and M. W. Bultman, Candidate penetrative fracture mapping of the Grand Canyon area, Arizona, from spatial correlation of deep geophysical features with surface lineaments, U.S. Geological Survey Data Series DS-121, 1 DVD disk, 2005.

Grauch, V. J. S., Statistical evaluation of linear trends in a compilation of aeromagnetic data from the southwestern U.S., *G. S. A. Abstracts with Programs*, **20**(7), A327, 1988.

Hancock, P., Fracture patterns in the Cotswold Hills, Proceedings Geolog-

ical Association, 80, 1969.

Hendricks, J. D. and G. M. Stevenson, Grand Canyon Supergroup: Unkar Group, in *Grand Canyon Geology*, edited by S. S. Beus and M. Morales, pp. 29–48, Oxford University Press, 1990.

Hereford, R. and P. W. Huntoon, Rock movement and mass wastage in the Grand Canyon, in *Grand Canyon Geology*, edited by S. S. Beus and M. Morales, pp. 443–460, Oxford University Press, 1990.

Hirschberg, D. M. and G. S. Pitts, Digital geologic map of Arizona: a digital database derived from the 1983 printing of the Wilson, Moore, and Cooper 1:500,000-scale map, U.S. Geological Survey Open-File Report 00-409, U.S. Geological Survey, Menlo Park, California, 2000.

Huntoon, P. W., Phanerozoic structural geology of the Grand Canyon, in *Grand Canyon Geology*, edited by S. S. Beus and M. Morales, pp. 261–309, Oxford University Press, 1990.

Jaeger, J. C. and N. G. W. Cook, *Fundamentals of Rock Mechanics*, Halsted Press, London, 585 pp., 1976.

Kandel, Abraham, Chapter 2: The algebra of inexactness, in *Fuzzy Techniques in Pattern Recognition*, pp. 22–90, John Wiley and Sons, Inc., U.S.A., 1982.

Kidwell, K. B., Global Vegetation Index User's Guide, U.S. Department of Commerce/National Oceanic and Atmospheric Administration/National Environmental Satellite Data and Information Service/National Climatic Data Center/Satellite Data Services Division, 1990.

Morales, M., Mesozoic and Cenozoic strata of the Colorado Plateau near the Grand Canyon, in *Grand Canyon Geology*, edited by S. S. Beus and M. Morales, pp. 247–260, Oxford University Press, 1990.

Nabighian, M. N., The analytic signal of two-dimensional magnetic bodies with polygonal cross-section. Its properties and use for automated anomaly interpretation, *Geophysics*, **37**, 507–517, 1972.

NASA, Landsat7, http://landsat.gsfc.nasa.gov/, accessed December, 2004, National Air and Space Administration, Washington, D.C, 2004.

Odling, N. E., P. Gillespie, B. Bourgine, C. Castaing, J.-P. Chiles, N. P. Christensen, E. Fillion, A. Genter, C. Olsen, L. Thrane, R. Trice, E. Aarseth, J. J. Walsh, and J. Watterson, Variations in fracture system geometry and their implications for fluid flow in fractured hydrocarbon reservoirs, *Petroleum Geoscience*, **5**, 373–384, 1999.

Potochnick, A. R. and S. J. Reynolds, Side Canyons of the Colorado River, Grand Canyon, in *Grand Canyon Geology*, edited by S. S. Beus and M. Morales, pp. 461–481, Oxford University Press, 1990.

Price, N. J., *Fault and Joint Development in Brittle and Semi-brittle Rock*, Oxford, Pergamon, 1966.

Price, N. J., The development of stress systems and fracture patterns in undeformed sediments, Proc. Third Congress of the International Society for Rock Mechanics, Denver, in Advances in Rock Mechanics, Vol. 1, Part A, 487–496, National Academy of Sciences, Washington D.C, 1974.

Richard, S. M., S. J. Reynolds, J. E. Spencer, and P. A. Pearthree, Geologic map of Arizona, scale 1:1,000,000, Arizona Geological Survey, Tucson, Arizona, 2000.

Robson, S. G. and E. R. Banta, Ground water atlas of the United States, Arizona, Colorado, New Mexico, Utah, HA 730-C, Colorado Plateau Aquifers, U.S. Geological Survey print publication, online version at http://capp.water.usgs.gov/gwa/index.html, 1995.

Sears, J. W., Geologic structure of the the Grand Canyon Supergroup, in Grand Canyon Geology, edited by S. S. Beus and M. Morales, pp. 71–82, Oxford University Press, 1990.

Sumner, J. S., Crustal geology of Arizona as interpreted from magnetic, gravity, and geologic data, in *The Utility of Regional Gravity and Magnetic Anomaly Maps*, edited by W. J. Hinze, pp. 164–180, Society of Exploration Geophysicists, Tulsa, Oklahoma, 1985.

Sweeney, R. E. and P. L. Hill, Arizona Aeromagnetic and Gravity Maps and Data, A Web Site for Distribution of Data, U.S. Geological Survey Open-File Report 01-0081, Version 1.0, http://pubs.usgs.gov/of/2001/ofr-01-0081/, 2001.

Thomas, R. W. and R. J. Huggett, *Modelling in Geography, A Mathematical Approach*, Barnes and Noble Books, Totowa, N.J., 338 pp., 1980.

USGS, National Elevation Dataset, http://ned.usgs.gov/, accessed December, 2004, U.S. Geological Survey, Reston, VA, 2004.

M. E. Gettings (e-mail: mgetting@usgs.gov) and M. W. Bultman